
Article:
Contreras-Arratia, R and Neuberg, JW orcid.org/0000-0001-7866-0736 (2019) Complex seismic sources in volcanic environments: Radiation modelling and moment tensor inversions. Journal of Volcanology and Geothermal Research, 381. pp. 262-272. ISSN 0377-0273

https://doi.org/10.1016/j.jvolgeores.2019.06.005

Complex seismic sources in volcanic environments: Radiation modelling and moment tensor inversions

Rodrigo Contreras-Arratia* and Jurgen W Neuberg

Institute of Geophysics and Tectonics, School of Earth and Environment, University of Leeds, Leeds LS2 9JT, UK

* Corresponding author at: Institute of Geophysics and Tectonics, School of Earth and Environment, University of Leeds, Leeds LS2 9JT, UK.

E-mail addresses: eerac@leeds.ac.uk (R. Contreras-Arratia), j.neuberg@leeds.ac.uk (J. Neuberg)

Abstract

Long period (LP) signals are special seismic events observed at volcanoes, which comprise both a high frequency onset due to brittle failure and a more energetic low frequency part due to resonance in a fluid-filled conduit. They are critical for volcano monitoring since they can be used as a volcanic forecasting tool. Classic seismology assumes planar faults for seismic sources; however, there is increasing evidence that suggests different fault shapes such as dyke faults and ring faults. We consider in this study narrow dykes and conduits rather than large calderas, hence, we model these complex sources by superposing vertical single double couple (DC) sources arranged along narrow fault structures with inner upward movement. We calculate seismic radiation patterns and synthetic seismograms for a rupture along a dyke, three different partial ring ruptures and a full-ring rupture. Results show that planar faults are the most effective at radiating energy. The more the source geometry deviates from a planar fault the smaller become the amplitudes and therefore the Moment Magnitudes. For example, the amplitudes decrease to 2.4% of the planar radiation for a full-ring rupture and to 0.7% for a dyke rupture. The waveforms produced by partial ring ruptures are in accordance to what is expected in the far field, representing the derivative of the source displacement and emulating radiation of a DC with different azimuths; however, the dyke and full-ring sources produce waveforms that appear to represent the second derivative of the source displacement and negative first onset polarisations. Moment Tensor Inversions support similarities between DC ruptures and partial ring ruptures; however, they show ambiguous solutions for the other sources. This point source assumption can lead to misinterpretations of slip history on the fault and a consistent underestimation of magnitudes which has direct

implications for magma ascent estimations derived from seismic amplitudes.

1. Introduction

At silicic volcanoes, dome collapse events and explosions are often preceded by increased activity of long period earthquake swarms (LP events); therefore, this type of seismicity can be used as a forecasting tool [6]. LP events comprise a high frequency onset (trigger) which provides the energy input for long period oscillations trapped in a fluid-filled structure to occur [10, 19]. The detailed interpretation of such low frequency seismic events often points to source models comprising the repeated expansion and compression of steam-filled, or ash-laden, sub-horizontal cracks explaining both the dominant frequency content and the seismic radiation pattern [16]. While such models explain the low frequency records adequately, the trigger source geometry is often geologically oversimplified e.g. simple planar faults. Furthermore, they fail to incorporate magma movement, ignoring the simultaneous observation of magma extrusion. The adoption of more realistic, alternative seismic source mechanisms based on brittle magma fracture [19] or stick-slip motion [11] at the conduit or dyke margins during magma ascent have been the subject of experimental and numerical endeavours in which more complex source mechanisms have been suggested. For example, a conical fault [9, 18, 24, 25] observed at regional and teleseismic distances was linked to a Compensated Linear Vector Dipole (CLVD) at a point source located at the centre of the cone.

Usually, seismic moment tensor (MT) inversions are the essential next step in shedding more light on the physical rupture processes involved. Classic inversions for a planar fault consider the fault size, orientation, and amount of slip as the main contributing factors controlling seismic amplitude patterns. For shear failure along a single fault plane the seismic moment (M_o) is directly proportional to both the area on which slip occurs and the amount of slip [2]; however, this might no longer apply for other fault geometries. Earthquake sources in volcanic areas have been studied by several authors, obtaining the full range of possible MT solutions. Besides double couple (DC) solutions [28, 1] they have found mass movement related sources; explosions/implosions (e.g. [22, 12, 5]), exploding/imploding cracks (e.g. [15]), CLVD (e.g. [24, 25]) and single forces (e.g. [21]). All these studies use the fundamental assumption behind classic MT inversions i.e. they are based on a planar surface geometry. The application to more complex seismic sources has so far been inconclusive.

Here, we advance existing source models from commonly used point sources on single fault planes, including the representation of a complex fault by a single point source, to spatially extended, more complex structures modelled by a combination of sources on the dyke margins. We consider five complex ruptures: a dyke rupture, three cases of failure along partial ring rupture and full ring rupture (Fig. 1). The seismic triggering is explained through the rupture of highly viscous magma that succumbs to high strain rates at the conduit walls [19], or as a friction-controlled stick-slip motion at the conduit margins [11]. Here, we solve the forward problem and obtain main features of seismic radiation patterns produced by these alternative source mechanisms in comparison to a single DC and CLVD. We found significant changes in amplitude, polarisation, and waveform (observation parameters) which have important implications when seismic data are interpreted in terms of magma movement e.g. slip history on the fault or maximum amplitude of slip. These implications become evident when solving the inverse problem.

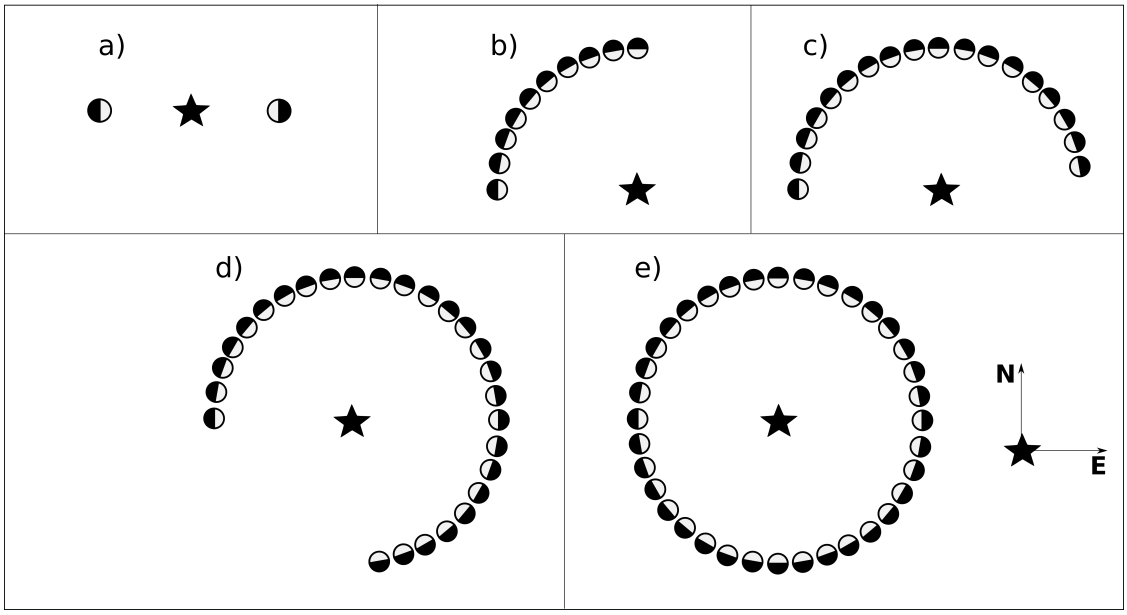

Figure 1: The five extended sources studied with focal mechanisms for each point source in plan view; a) Dyke fault, comprising two opposed DC. b) 1/4-ring fault, comprising 9 point sources. c) 1/2-ring fault, consisting of 18 point sources. d) 3/4-ring fault, 27 point sources. e) Full-ring fault, 36 point sources. Each point source is acting within an area patch. The star represents the reference point for each case.

2. Modelling complex sources by superposition of point sources

In order to represent these complex sources we superimpose simultaneously acting DC sources on "patches" arranged along the shape of non planar narrow ruptures. Each point source is represented by a DC moment tensor with a vertical fault and vertical rake, azimuths vary depending on the shape; upward movement is always in the inner part of the structure representing magma ascent. For the first time, we model slip on: (i) a dyke fault with 2 patches, (ii) 1/4-ring with 9 patches, (iii) 1/2-ring with 18 patches, (iv) 3/4-ring with 27 patches and (v) a full-ring with 36 patches. The number of patches was chosen to satisfy the sampling theorem using the velocity and frequency as listed in Table 3. Hence, for narrow structures considered here the contributions of all sources arrive in a short time interval compared to the period. Since our complex seismic sources are represented by individual sources, the spherical coordinates $(r_{ij}, \theta_{ij}, \phi_{ij})$ (observation parameters, i.e. distance, take-off angle and azimuth, respectively) from the j-th source to the i-th seismic station vary slightly. For each complex source we define a reference point (star in Figs. 1 and 2) and find analytical expressions linking the observation parameters between each single point source and a seismic station $(r_{ij}, \theta_{ij}, \phi_{ij})$ to the equivalent observation parameters between the reference point of the entire complex source and this particular station $(r, \theta, \phi)_i$, as shown in Fig. 2.

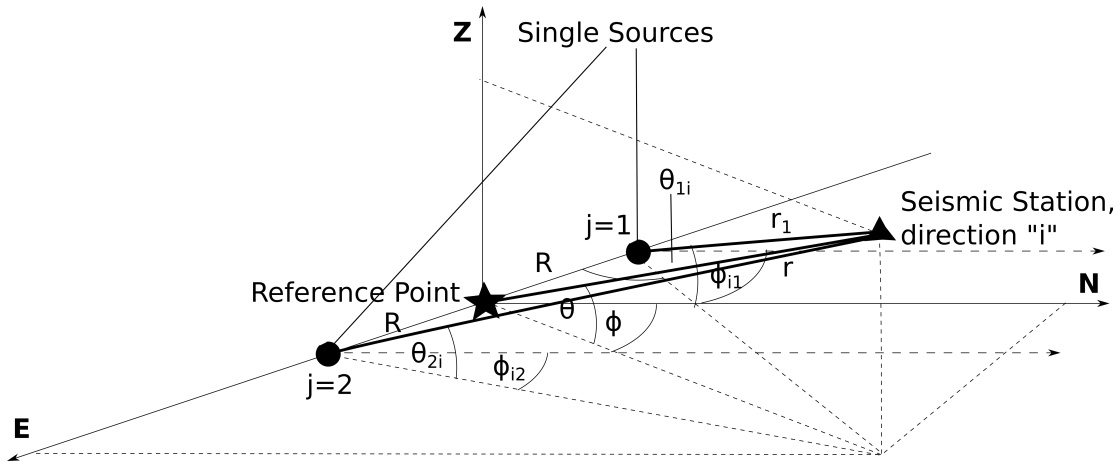

Figure 2: Coordinate system used showing the reference point (star) for a dyke comprising two DC sources (circles; j=1,2) and a seismic station (triangle). The observation parameters related to the seismic source are a function of the equivalent parameters related to the reference point, i.e. $r_1 = r_1(r, \theta, \phi)$, $\theta_1 = \theta_1(r, \theta, \phi)$, $\phi_1 = \phi_1(r, \theta, \phi)$, $r_2 = r_2(r, \theta, \phi)$, $\theta_2 = \theta_2(r, \theta, \phi)$ and $\phi_2 = \phi_2(r, \theta, \phi)$.

$$r_{ij} = \sqrt{r^2 + R^2 + 2rR\cos\theta\cos\phi}$$
$$\theta_{ij} = \arctan\left(\frac{r\sin\theta}{\sqrt{(r\cos\theta)^2 + R^2 + 2rR\cos\theta\cos\phi}}\right)$$
$$\phi_{ij} = \arctan\left(\frac{\sin\phi}{\cos\phi + \frac{R}{r\cos\theta}}\right) \quad (1)$$

We can estimate the P-wave Radiation Pattern for a single DC in a spatial grid (θ, ϕ), using $a_{ij} = \sin 2\theta_{ij} \cos\phi_{ij}$ which gives us the radiation pattern produced by the j-th source at a certain direction $(\phi, \theta)_i$. Then, we sum all contributions produced by each source in angle increments of δ [°] in order to span all space and calculate the net amplitude expected for P-waves in all directions. In this case i runs over the 3D space in angular increments of δ to consider all different directions. We assume that all the phases from different point sources arrive simultaneously at the station i.e. we use a long wavelength approximation, as the distance between sources $(2R)$ is very small compared to the source-station distance (r). Integration steps and boundaries depend on the shape of the source and are shown in Table 1. Note that all cases considered in this study use $R << r$, where $R = 20$ m represents a typical size for a narrow conduit geometry. The modelling of the seismic wavefield of larger volcanic structures, e.g. calderas, where seismic sources would be distributed along ring faults with much longer radius, hence, $R \sim r$, show that the wavefield and radiated amplitude will have different characteristics and their analysis is beyond the scope of this article.

Source	Lower boundary for summation, ϕ_1	Upper boundary for summation, ϕ_N	No. of Point Sources (N)
Dyke	0°	180°	2
1/4-ring	90°	180°	9
1/2-ring	0°	180°	18
3/4-ring	−90°	180°	27
Full-ring	0°	0°	36

Table 1: Parameters for numerical integration.

We calculate the net Radiation Pattern for M sources with,

$$A_{\mathrm{p}} = \sum_{j=1}^{M} \sum_{i=1}^{N} \sin\left(2\theta_{ij}\right) \cos\left(\phi_{ij}\right) \quad , \text{ with } \theta_{ij} = \theta_j + i\delta \text{ and } \phi_{ij} = \phi_j + i\delta \qquad (2)$$

where A_{p} is the relative P-wave amplitude compared to a normalised single DC, N the number of directions (ϕ, θ) considered and δ denotes the angular increments in space.

However, this integration process does not consider travel time differences caused by the slight differences in source-receiver distances for different sources at the same station we calculate synthetic seismograms to take this effect into account. We use the software QSEIS [27] to produce synthetic signals in a homogeneous half-space in order to obtain the direct influence from the source, avoiding effects of the medium. We use a 5 Hz simulated delta pulse (f) as the slip on the fault, for each point source; parameters for modelling are shown in Table 2. "Recording stations" are located in circular grids in every 500 m epicentral distance, up to 5 km and every 30° azimuth, however, for the moment tensor inversions we use 3 concentrical rings at 1, 2 and 3 km (Fig. 3). Hence, we have 120 stations sampling at a frequency of 100 Hz and we use 36 for inversion. We obtain synthetic seismograms from each contributing DC source using values for the observation parameters given in Eq. 1 and the source-station configuration. Next, we sum up all the waveforms generated at each point source to obtain the net waveform produced by the respective ruptures in all stations.

Later, we quantify their main features such as amplitude of first arrival, polarisation and the waveform itself; we compare them with the ones produced by a simple DC and a Compensated Linear Vector Dipole (CLVD), both of magnitude $M_w = 2.2$. We first obtain amplitudes that have been generated by using different number of patches, i.e. different fault surface sizes. In order to compare the "efficiency" of all rupture models, we need to calculate the seismic radiation produced by the same areas, slips and shear coefficient with different shapes. To achieve this we normalise the waveforms by the number of sources/patches involved in each case.

V_p	q_p	V_s	q_s	R_{dyke}	R_{ring}	M_w	Depth Event	Frequency
3000 m/s	1000	1732 m/s	1	10 m	20 m	2.2	1 km	5 Hz

Table 2: Parameters for forward modelling.

Using the datasets created in the forward modelling for the five sources listed above, we perform "classic" moment tensor inversions under the assumption of a

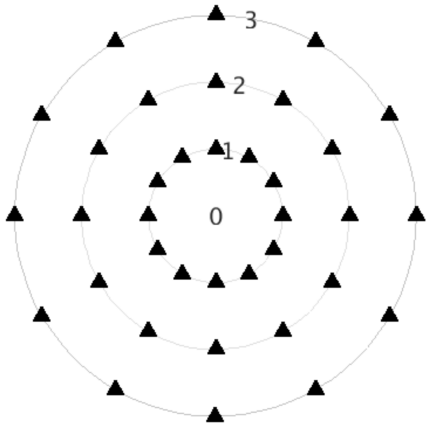

Figure 3: "Recording stations" used for inversion in this study, located in 3 rings, 1-3 km from the rupture models at the centre.

point source on a simple fault plane, which is the most common approach in volcano seismology. The inversions were carried out using the Kinematic Waveform Inversion Tools (KIWI) [4] which uses the Levenberg-Marquardt method to solve the inverse problem [17]. This inversion returns a full moment tensor comprising the isotropic and deviatoric components, the latter of which is further decomposed into double couple (DC) and compensated linear vector dipole (CLVD). Single force components are calculated along with moment tensor components using the software package VOLPIS, which gives us the source time functions for the 9 components (6 moment tensor components + 3 single force components [3]). Here we find only an "*apparent solution*" by applying standard moment tensor inversion techniques to a curved, more complex fault. These apparent solutions can now be compared to real data examples.

Finally, we want to explore the effect of the radius of curvature in the radiation, specifically, in the maximum amplitude obtained in a particular station. We model 1/4-ring ruptures with different radius of curvature with same location for the central point. The recording station is located 6 km away forming a perpendicular line to the tangent of the curved surface at the central point of the fault (Fig. 4a).

2.1. Seismic radiation patterns and amplitudes

In this section we calculate main features of the seismic radiation pattern produced by complex-shaped faults (Fig. 1). These are calculated as described in the previous section using Equations (1) and parameters in Table 1. If the dimension

of the complex source is small compared to the seismic wavelength and, therefore, the differential travel times are negligible, we can obtain an estimation of the radiation pattern assuming simultaneously arriving P-waves at a single station. This corresponds to observations at regional and teleseismic distances, which can also be considered a long wavelength approximation. On the other hand, when travel time differences between sources are considered, corresponding to a short wavelength approximation, the waveforms will be affected. For comparison, in Fig. 5a and b, we show the radiation patterns, polarisations at the surface, waveforms and focal mechanisms for a vertical DC and a vertical CLVD in the far field, respectively.

Radiation patterns (long wavelength approximation) for dyke and full-ring ruptures are shown in Fig. 5c and g, they look similar to a single force acting upwards. For the dyke rupture, lobes are elongated along the dyke's axis with small lobes perpendicular to this axis, which can be observed in very narrow areas. In addition, for the full-ring rupture, lobes are axially symmetric. Therefore, we expect positive first arrivals in the vicinity of the epicentre when all contributions arrive at the same time. For partial ring ruptures we obtain radiation patterns similar to DC ruptures with different orientations, as shown in Fig. 5d, e and f. We further discuss them below.

We calculate synthetic seismograms (short wavelength approximation) for all rupture types and we select the stations with the largest amplitudes at 1 km epicentral distance. These synthetic amplitudes are computed for ruptures with different number of point sources. Even without normalising the amplitudes of the overall fault area involved, dyke and full-ring ruptures produce the smallest amplitudes among the complex sources due to the high amount of destructive interference. For partial ring ruptures we obtain radiation patterns similar to DC ruptures; moreover, the amplitudes do not increase linearly with the fraction of fault area that fails, but the highest amplitude is obtained for half-ring rupture, while amplitudes for 1/4-ring and 3/4-ring ruptures are smaller and similar (Fig. 6a). Note, that despite the increasing slip surface from 1/4- to 3/4-ring ruptures the amplitude remains similar due to a higher proportion of negative interference in the case of the 3/4-ring rupture which affects the overall efficiency of radiated energy from these sources. These amplitude differences are crucial for the calculation of moment magnitude of the events during the inversion process.

In order to quantify the "efficiency" of each source type we compare the amplitudes with the maximum amplitude produced by a single DC with the same surface slip area i.e. we calculate the maximum amplitudes of first onsets at 1 km epicentral distance and normalise them to the area of rupture for each case. With these results we compare the radiation emitted by sources with the same area but different shapes

(Fig. 6b). The maximum amplitude of the first arrival at 1 km distance produced by a 1/4-ring rupture is reduced to 89% of the amplitude produced by a DC. For 1/2-ring rupture the reduction reaches 63% and for 3/4-ring rupture the amplitude is reduced to 30%. The waveforms and polarisations obtained are in agreement with far field DC radiation; the 1/4-ring rupture shows similar radiation with a 45° striking vertical DC, the half-ring rupture similar to a vertical DC with strike of 90° and the 3/4-ring rupture with a 135° striking vertical DC (Fig. 7).

The similarity between these partial ring ruptures and their corresponding planar fault is due to the fact that the contribution of point sources at the flanks of the rupture are responsible for the negative interference, reducing the resulting amplitude, while the sources at the central zone of the partial ring contribute most of the radiated energy. Hence, the direction of maximum radiation is defined by the normal to the alignment of the sources in the central zone (Fig. 7). The general amplitude behaviour is dependent on the symmetry and dimension of the complex sources and will be further reviewed in the discussion section.

For the dyke and full-ring rupture we obtain a further amplitude reduction to only 0.7% and 2.4%, compared to a single DC, respectively (Fig. 6b). Results of the modelling are summarised in Fig. 5. Note that this behaviour is observed only for strong curvatures, here, for example for a small conduit radius (20 m) or narrow dyke (10 m), later we will investigate the impact of fault curvature.

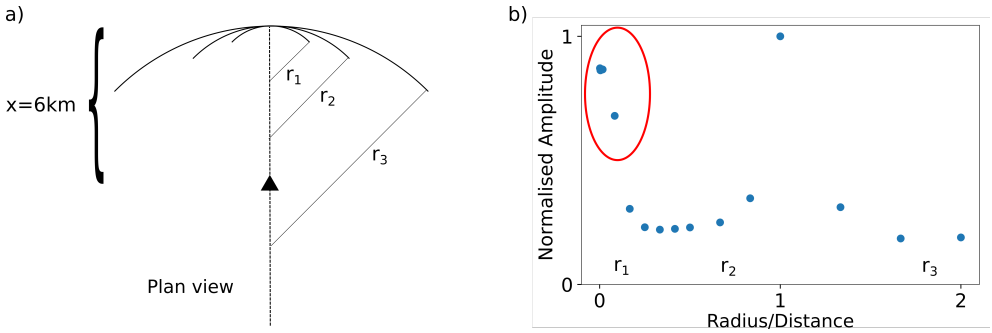

Figure 4: a) Geometries used to quantify the curvature dependence on amplitudes, station fixed at 6 km while the radius of curvature varies. b) Normalised amplitudes for different curvatures are smaller than a DC, except when the seismic station is located at the centre of the ring structure at $r = 6$ km and perfect focusing effect occurs. The circle shows the case of study for narrow dykes.

2.2. Waveforms: travel time differences

In this section, we focus on the polarisations and waveforms for each source type, now taking travel time differences between individual sources into account, hence

using a short wavelength approximation. Synthetics are calculated as described in the previous section using Eqs. (1) and parameters in Table 1. The slip on the fault is modelled by a simulated delta function (f) at 5 Hz cut-off frequency; therefore, we expect for each contribution, far field waveforms proportional to the first derivative of the slip on the fault ($\dot{f}$).

The synthetic seismograms obtained for partial ring rupture show that the waveforms represent the first derivative of the displacement on the fault ($\dot{f}$), as expected. Hence, the configuration of sources in this case does not affect significantly the waveforms. On the other hand, the synthetic seismograms for dyke and full-ring ruptures are proportional to the second derivative of the slip on the fault ($\ddot{f}$), which differs from that expected for a point source (Fig. 8). Due to interference of sources of opposite polarisation in close proximity e.g. dyke rupture, the waveforms $u(t)$ show an additional differentiation effect. Hence;

$$u(t) \propto \left[\dot{f}(t) - \dot{f}(t+dt)\right] \quad \propto \quad \ddot{f} \quad , \text{ if } dt \to 0 \tag{3}$$

where dt corresponds to the travel time difference between the two sources on opposite sides of the dyke rupture or full-ring rupture; hence, for small dt the superposition of these two sources introduces an apparent time derivative. A special case is the waveform produced by a 3/4-ring rupture where two opposed quarter ruptures produce this double differentiated signal, i.e. NW and SE quarters; however, its amplitude is much smaller than the produced by the remaining quarter (NE) which dominates the signal with a waveform proportional to $\dot{f}$, emulating the case of a 1/4-ring rupture with 135° azimuth (Fig. 7).

Although the magmatic process to produce these synthetic seismograms is related to an overpressure in the plumbing system which drives magma ascent, the polarisations for the dyke and the full-ring ruptures show negative first onsets. Note that for a single source this negative polarisation would be linked to an implosion or a closing crack, i.e. a geological structure collapsing due to lack of pressure.

2.3. Effect of the curvature on the seismic radiation

So far we have investigated the effect of different angular ruptures on the net radiation, using a fixed 20 m radius using recording stations outside the ring. In this section we use the direction of maximum amplitude for curved ruptures (Fig. 4a) in order to evaluate the relation between amplitude and the radius of curvature.

We calculate the radiation of a 1/4-ring rupture with different curvatures arriving at a station fixed at 6 km away from the ruptures's centre point (Fig. 4a). Using the radius of curvature r and the distance from station to fault d, we can generalised the results and identify three cases depending on the value of the ratio r/d: for $r/d < 1$

the station is located outside the ring structure, for $r/d > 1$ is located within the structure, while for $r/d = 1$ is located in the centre of the ring.

We show in Fig. 4b that the amplitudes for stations outside the ring structure reach almost the maximum amplitudes possible due to the constructive interference between single sources. For larger ring faults, hence $r/d \rightarrow 1$, the amplitude of radiation decays about 5 times the maximum amplitude due to the combination of geometrical effects and wavelength interference. An important focusing effect is observed when the station is placed in the centre of the ring fault $r/d = 1$, reaching the maximum value; this is the only point where travel time differences are zero, i.e. all the contributions arrive at the same time and interfere constructively. Amplitudes decrease again when the station is placed even closer to the fault $r/d > 1$, increasing destructive interference. This shows that amplitudes behave differently when stations are located inside and outside the ring fault, increasing the variability of possible moment tensor solutions and magnitudes.

All these ruptures produce signals that might have been observed in nature and they could have an interpretation in terms of the classic view of moment tensor inversion. Some of these interpretations were made considering first arrivals instead of the full waveform, and therefore they may be an oversimplification for magma ascent processes. For the moment tensor inversion carried out here, we show that the classic approach will provide a solution based on a single point source, fitting the "best" moment tensor solution in the established scheme; however, it does not point to the actual physical process. We will prove in the next section that this method systematically underestimates the magnitude and misinterprets the slip on the fault.

3. Inverse modelling

The synthetic seismograms considered in the following are the superposition of the waveforms produced by each point source which interfere with each other. This interference can be constructive or destructive, depending on individual radiation patterns and travel time differences. In all cases, the time series are distorted at different levels; dyke and full-ring ruptures introduce an additional time derivative in the waveforms and the amplitudes change drastically. Moreover, partial ring ruptures maintain the waveforms expected from a single source, while amplitudes and location of nodal planes change significantly. Therefore, this interference introduces apparent changes in source parameters and magnitude calculations, which need to be quantified and eventually corrected. We perform moment tensor inversions in order to obtain source parameters for each source using the classic approach i.e. assuming a point source with planar geometry. The KIWI software [4] provides moment

tensor components and computes the fraction of this solution which represents both isotropic and deviatoric parts; the latter is decomposed in a DC and CLVD solution. Thus, we treat these spatially extended sources as a simple planar fault; which, however, does not consider the physics involved.

To perform the moment tensor inversion we use a subset of 36 "recording stations" that are deployed in 3 concentric rings at 1 km, 2 km and 3 km distance and an ideal azimuthal coverage every 30°. It is important to note that each point source used in the forward modelling are vertical DC's with $M_w = 2.2$. For comparison with the ruptures studied, Fig. 5a and b show radiation patterns, polarisations at surface, waveforms and focal mechanisms for a single DC rupture and CLVD, respectively.

Fig. 5c shows main features of radiation for the dyke rupture, radiation pattern, polarisations at surface and waveforms. Synthetic seismograms show negative first onsets in the stations to the east and west from the epicentre, in addition to amplitudes tending to zero in the north and south. No positive first onsets are obtained. The MT solution shows an 87% isotropic component, 10% DC and 3% CLVD; in addition, the calculated magnitude of the event is $M_w = 1$. This MT result assumes a point source and assigns positive polarisations to the north and south, which does not match the synthetics.

For partial ring rupture cases (Fig. 5d, e and f) we observe similarities with DC radiation. Accordingly, the MT solutions are dominated by vertical DC components ($> 90\%$). We obtain different fault azimuths for different ruptures modelled, which are in agreement with polarisations observed, e.g. 45° for 1/4-ring rupture, 90° for 1/2-ring rupture and 135° for 3/4-ring rupture. However, the maximum amplitudes are different in each case; the magnitude for the case of 1/2-ring rupture shows an apparent Moment Magnitude of 2.9. Moreover, despite the differences in areas of rupture, the cases of 1/4-ring rupture and 3/4-ring rupture show the same magnitude of $M_w = 2.8$.

Fig. 5f shows results of the full-ring rupture. Only negative first onsets are observed, despite the radiation pattern showing a positive lobe just above the hypocentre. The moment tensor inversion given by KIWI results in a vertical CLVD point source; however, this is fundamentally different as far as polarisations are concerned; the CLVD solution assigns positive first arrivals to the stations at 1 km distance which actually show negative onsets. Thus, this solution minimise the misfit during the inversion process, but it does not represent at all the physics of the source process. In addition, the MT solution is,

$$\begin{pmatrix} -1.543778 & -0.002433 & -0.003922 \\ -0.002433 & -1.546797 & -0.002606 \\ -0.003922 & -0.002606 & -1.032088 \end{pmatrix} \times 1.8 \cdot 10^{12} \text{ Nm}$$

still indicating 80% isotropic component; while the 20% remaining is CLVD. In this case, the graphic representation of the result is misleading since it looks like a vertical CLVD; however, the diagonal components are all negative, hence it is interpreted as an imploding volume.

Moreover, the inversion procedure integrates the waveforms observed in the far-field to obtain the correct source slip at the fault. For cases of partial rupture, this point source approach returns the correct slip on the fault. However, for the cases of dyke rupture and full-ring rupture, the moment tensor inversion returns the derivative of the actual source slip at the fault. Hence a double integration would be necessary to retrieve the correct source time history.

4. Discussion: implications for volcano seismology

This theoretical and numerical approach attempts to provide the fundamental features of the radiation patterns, i.e. waveforms, polarisations and amplitudes for non-planar faults and compare them with point sources. Furthermore, from synthetic seismograms we obtain moment tensor solutions assuming a point source rupture.

4.1. Classic view fails

The study of these scenarios demonstrates that the added complexity of volcanic seismic sources leaves a much wider space for interpretation of the actual source process. This has important consequences if classic moment tensor inversion techniques, based on the point source assumption, are used to estimate magma ascent rates from earthquake swarms. Due to interference, a complex rupture of any shape will always produce seismic amplitudes that are smaller than any planar slip surface of equivalent size and slip; in addition, the actual values for amplitudes depend on the trade-off between wavelength and curvature of the structure. If a spatially extended source is assumed as a point source, the discrepancies in P-wave amplitudes will lead to an underestimation of the rate at which magma rises in the volcanic conduit. For example, the moment tensor inversion of the full-ring rupture case can result in an underestimation of the seismic moment M_o by a factor of ~ 42. The underestimation of M_o leads to an underestimation of slip on the fault and a consequently underestimation of magma flow rate in depth which may have severe implications for eruption forecast. Hence, we are assuming less magma moving upwards in the system.

If the nature of the source and its seismic moment M_o are known, magma ascent rates can be inferred from measured seismic amplitudes. By advancing towards inversion techniques that allow for spatially extended source mechanisms, the amount of slip occurring in the conduit can be calibrated. These inversion techniques need to be able to analyse the full waveform obtained, not only the first arrivals in order to address the differences in waveforms we obtained for the cases of dyke and full-ring ruptures. For these cases we obtain a waveform which appears to be the second derivative of the slip function on the fault, introducing a critical problem when using classic moment tensor inversions since these methods integrate waveforms only once to retrieve the slip function. This leads to a mis-interpretation of the slip history at the fault, which in volcanic environments can have huge implications. If we observe $\ddot{f}$ at the stations, a point source inversion scheme will interpret the slip on the fault as $\dot{f}$ which means an oscillating magma column while the model was based on a simple upward motion followed by relaxation (Fig. 9).

The calibration of individual volcanic systems by comparison of observed seismic amplitudes and magma extrusion rates is therefore crucial to obtain accurate magma flow rates along extended fault planes, and once successfully calibrated this will contribute towards identifying a critical value of magma flow rate that may lead to dome collapse [26]. Moreover, unless a volcanic edifice is covered by a very dense seismic network providing sufficient input for the inversion of a higher order moment tensor, in a suitable geometry [13]. it is very unlikely that the true mechanism of a complex volcanic seismic source can be determined in a unique way. In addition, caution should be applied if classic moment tensor inversions return CLVD, DC or single force component mechanisms with large uncertainties; magma ascent rates determined in such way should be considered lower bounds only.

4.2. Are the signals observed generated by complex sources?

In contrast to automatically assuming point sources and planar faults, we suggest to consider other rupture shapes to explain the seismic observations, which show high levels of uncertainty and might be generated within a volcanic environment. However, how can we gather enough evidence to select complex ruptures approach and discard planar fault rupture?

For the case of dyke and full-ring ruptures we expect negative polarisations at all stations; however, they have different properties than an implosion or imploding cracks. For example, the dyke rupture shows a nodal plane along its projection at the surface, and the amplitude pattern is unique for these kind of ruptures. For the full-ring rupture, waveforms show radial symmetry with amplitudes that increase in the first kilometre, for a 1 km depth source. Moreover, the waveforms modelled can

be more easily explained with complex ruptures.

A scheme of the different situations assuming different slip on the fault is shown in Fig. 9, explaining the integration process needed to retrieve the correct slip history at the fault. Note that the function f was selected for this study since the modelled displacement (Fig 9a - 3rd waveform) has similarities with velocity seismograms in nature when the slip on the fault is modelled as a step function (Fig 9b - 5th waveform). On the other hand, the same waveforms can be explained as far field velocity records produced by a planar fault if we assume a displacement on the fault given by a simulated delta function (Fig 9c - 4th waveform). However, tectonic or magmatic tractions cannot change direction so fast and easily, and a net displacement on the fault is needed when magma is moving upwards or eventually being extruded. Thus, the most suitable function to describe slip on the fault is still the step function. Some studies have considered source time functions described by a simulated delta function to explain the data, which can be a possible mechanism for very long period pressurisation and depressurisation of the system [7, 14] but not LP trigger signals.

Due to the radial symmetry, polarisations obtained for full-ring rupture are similar to the ones produced by a single vertical force which are often used in moment tensor inversions in volcanic environments. We perform moment tensor inversions, obtaining simultaneous solutions for moment tensor and single force components which returns for the full-ring radiation the superposition of a downward single force and a vertical CLVD (Fig. 10). Hence, the isotropic components obtained previously are now replaced by a vertical single force. A significant contribution attributed to a single force (plus CLVD) could give an indication that a complex source such as a ring fault should be considered, particularly if the observed displacement at the source indicates an additional derivative of an expected upwards motion by magma ascent. In this light, single force inversions would decrease the misfits, however, without explaining the physics of the source adequately and still the displacement at the fault would be misinterpreted.

4.3. Full-ring rupture as CLVD?

By numerical integration along the conduit walls we obtain the radiation patterns depicted in Fig. 5. For comparison, they are shown together with the classic vertical double couple solution and the pattern for a compensated linear vector dipole (CLVD). The radiation pattern for the full-ring rupture shows axial symmetry about the vertical axis, and consists of a large compressional lobe directly above the source and an inversely polarised, dilatational lobe with the same amplitude below it. The observed radiation patterns of ring fault and CLVD source are remarkably similar in the upper hemisphere, but are fundamentally different as a whole. Their distinction

in volcanic settings, however, is likely to be very difficult. For both, CLVD and full-ring rupture, the nodal planes lie off the fault axes, and the transition from compressional to dilatational first motion is, therefore, dependent on the source depth of the event. Due to the shallow source depths of most volcano seismic events, the generally narrow aperture of seismic networks on volcanoes, and small (< 3) event magnitudes, only seismicity radiated at limited take-off angles above the source will likely be detected. This means that the radiation of the trigger should not be observed at distant stations e.g. in our modelling of the full-ring rupture, the amplitudes observed at the closest stations (500 m) decay by a factor of 12 compared to the stations at 5 km. Generally, given a specific topography and station distribution the two fundamentally different physical processes for the trigger, ascending magma in the conduit represented by the full-ring fault model on the one hand, and a CLVD model on the other hand, may result in the same observed P-wave polarities with almost indistinguishable radiation patterns.

Seismic signatures observed at Nyiragongo volcano, D. R. Congo, between 2002 and 2005 exhibited a radiation pattern showing downward motion in the centre and upwards motion around it [23]. These events were interpreted as caused by slow slip on an invert dipping ring fault [9], and labelled as CLVD. Similarly, in 2014, seismic events were detected on Barðarbunga volcanic complex, Iceland, comparable to those observed in 1995, which had been associated with slip on at least a part of a ring fault and described as having a CLVD component [18]. In these cases a CLVD component was generated by invert raking conical fault planes and their seismic signature was observed in the far-field as regional events. By inverting long-period seismic data, the epicentre would be determined in the centre of the ring fault, but not along the fault. CLVD and ring ruptures are fundamentally different source mechanisms which require different interpretations. A CLVD is caused by redistribution of volume, e.g. the drainage of magma from a chamber into a sill. In contrast, the motion of a ring fault could be interpreted as ascending or descending magma without conserving the overall volume. Furthermore, only for long period seismic waves (> 10 s), such as observed at Nyiragongo, an instantaneous motion on an entire ring fault with a radius of several kilometres can produce a superposition of seismic waveforms that would produce the observed radiation pattern and locate in the centre of such a ring fault. Where earthquake locations coincide with the caldera rim, as in the case of Barðarbunga, we demonstrated that slip on only parts of a caldera rim would result DC radiation pattern, let alone the discrepancy between the frequency content of the superimposed seismic waveform and the dimension of the caldera of more than (> 10 s). Locally limited drainage of magma pockets rather than a simultaneous collapse of an entire caldera could produce such seismic signatures.

5. Conclusions

Geological observations of different fault shapes have been reported in volcanic environments, which deviate from planar faults. We demonstrate that MT inversions for these ruptures can underestimate the magnitude of the event and misinterpret the slip on the fault when we adopt the classic view of point sources. MT inversion software packages will calculate the best fitting solution between DC, CLVD and Isotropic components or combinations of them, even if the geometry of the fault and the physics of rupture are not well defined.

The misinterpretation of the slip on the fault can introduce ambiguity in the estimations of magma ascent. Since the fractures occur in the magma body, the seismic slip represents the time history of magma ascent. If we record a full-ring rupture with broadband seismometers in the surroundings of the event, and we treat it as a point source, we obtain as the slip on the fault a simulated delta function, hence, an upward and downward motion. This means that the magma seems to ascend in the first part, and then falls back to its original position; therefore, no net ascent is taking place. This is in contrast to the step-wise magma ascent actually taking place which leads to a fundamentally different source process.

The impact of underestimating the magnitude is critical for magma ascent estimation, since a smaller magnitude implies smaller slip, hence a smaller ascent rate.

The polarisation of first onsets observed for full-ring rupture are axially symmetric, similar to a negative CLVD or downward single force but not exactly the same; it is very difficult in real observations to differentiate between those interpretations due to the limited number of instruments in seismic networks. The dyke ruptures can be spanned as closing cracks using the point source approximation, which is completely different physical mechanism. Moreover, we expect DC solutions for partial-ring rupture; so far there is no seismological methodology capable of differentiate between a planar fault and a partial-ring rupture.

A theory is needed, which can address differences between spatially extended sources with different fault geometries and predict radiation features analytically. This can include higher order moment tensor solutions [8] or a finite fault approach [20]. Ambiguous results during inversion methods should be interpreted as an indication that complex sources might be at work. Data have to be compared with synthetics in order to inspect different ruptures. Finally, it is of major importance that the MT solutions and focal mechanisms include the study of full waveforms, instead of considering only first arrival polarisations, since the waveforms could be affected by interference patterns due to a complex source geometry.

6. Acknowledgements

This PhD research project is funded by CONICYT Chile through its scholarship program Becas Chile (72170194). Jurgen Neuberg is partially funded by the Centre for the Observation and Modelling of Earthquakes, Volcanoes and Tectonics (COMET NE/J01978X/1).

References

[1] Ágústsdóttir, T., Woods, J., Greenfield, T., Green, R.G., White, R.S., Winder, T., Brandsdóttir, B., Steinthórsson, S., Soosalu, H., 2016. Strike-slip faulting during the 2014 bárðarbunga-holuhraun dike intrusion, central iceland. Geophysical Research Letters 43, 1495–1503.

[2] Aki, K., Richards, P.G., 2002. Quantitative seismology. volume 1.

[3] Cesca, S., Dahm, T., 2008. A frequency domain inversion code to retrieve time-dependent parameters of very long period volcanic sources. Computers & Geosciences 34, 235–246.

[4] Cesca, S., Heimann, S., Stammler, K., Dahm, T., 2010. Automated procedure for point and kinematic source inversion at regional distances. Journal of Geophysical Research: Solid Earth 115.

[5] Chouet, B., Dawson, P., Ohminato, T., Martini, M., Saccorotti, G., Giudicepietro, F., De Luca, G., Milana, G., Scarpa, R., 2003. Source mechanisms of explosions at stromboli volcano, italy, determined from moment-tensor inversions of very-long-period data. Journal of Geophysical Research: Solid Earth 108.

[6] Chouet, B.A., 1996. Long-period volcano seismicity: its source and use in eruption forecasting. Nature 380, 309.

[7] Chouet, B.A., Matoza, R.S., 2013. A multi-decadal view of seismic methods for detecting precursors of magma movement and eruption. Journal of Volcanology and Geothermal Research 252, 108–175.

[8] Dahm, T., Krüger, F., 1999. Higher-degree moment tensor inversion using far-field broad-band recordings: theory and evaluation of the method with application to the 1994 bolivia deep earthquake. Geophysical Journal International 137, 35–50.

[9] Ekström, G., 1994. Anomalous earthquakes on volcano ring-fault structures. Earth and Planetary Science Letters 128, 707–712.

[10] Ferrazzini, V., Aki, K., 1987. Slow waves trapped in a fluid-filled infinite crack: Implication for volcanic tremor. J. geophys. Res 92, 9215–9223.

[11] Iverson, R.M., Dzurisin, D., Gardner, C.A., Gerlach, T.M., LaHusen, R.G., Lisowski, M., Major, J.J., Malone, S.D., Messerich, J.A., Moran, S.C., et al., 2006. Dynamics of seismogenic volcanic extrusion at mount st helens in 2004–05. Nature 444, 439.

[12] Kumagai, H., Placios, P., Ruiz, M., Yepes, H., Kozono, T., 2011. Ascending seismic source during an explosive eruption at tungurahua volcano, ecuador. Geophysical Research Letters 38.

[13] Lanza, F., Waite, G.P., 2018. A nonlinear approach to assess network performance for moment-tensor studies of long-period signals in volcanic settings. Geophysical Journal International 215, 1352–1367.

[14] Lyons, J.J., Waite, G.P., 2011. Dynamics of explosive volcanism at fuego volcano imaged with very long period seismicity. Journal of Geophysical Research: Solid Earth 116.

[15] Mildon, Z.K., Pugh, D.J., Tarasewicz, J., White, R.S., Brandsdóttir, B., 2016. Closing crack earthquakes within the krafla caldera, north iceland. Geophysical Supplements to the Monthly Notices of the Royal Astronomical Society 207, 1137–1141.

[16] Molina, I., Kumagai, H., Yepes, H., 2004. Resonances of a volcanic conduit triggered by repetitive injections of an ash-laden gas. Geophysical Research Letters 31.

[17] Moré, J.J., 1978. The levenberg-marquardt algorithm: implementation and theory, in: Numerical analysis. Springer, pp. 105–116.

[18] Nettles, M., Ekström, G., 1998. Faulting mechanism of anomalous earthquakes near bárdarbunga volcano, iceland. Journal of Geophysical Research: Solid Earth 103, 17973–17983.

[19] Neuberg, J.W., Tuffen, H., Collier, L., Green, D., Powell, T., Dingwell, D., 2006. The trigger mechanism of low-frequency earthquakes on montserrat. Journal of Volcanology and Geothermal Research 153, 37–50.

[20] Olson, A.H., Apsel, R.J., 1982. Finite faults and inverse theory with applications to the 1979 imperial valley earthquake. Bulletin of the Seismological Society of America 72, 1969–2001.

[21] Richardson, J.P., Waite, G.P., 2013. Waveform inversion of shallow repetitive long period events at villarrica volcano, chile. Journal of Geophysical Research: Solid Earth 118, 4922–4936.

[22] Ruiz, M.C., Lees, J.M., Johnson, J.B., 2006. Source constraints of tungurahua volcano explosion events. Bulletin of volcanology 68, 480–490.

[23] Shuler, A., Ekström, G., 2009. Anomalous earthquakes associated with nyiragongo volcano: Observations and potential mechanisms. Journal of Volcanology and Geothermal Research 181, 219–230.

[24] Shuler, A., Ekström, G., Nettles, M., 2013a. Physical mechanisms for vertical-clvd earthquakes at active volcanoes. Journal of Geophysical Research: Solid Earth 118, 1569–1586.

[25] Shuler, A., Nettles, M., Ekström, G., 2013b. Global observation of vertical-clvd earthquakes at active volcanoes. Journal of Geophysical Research: Solid Earth 118, 138–164.

[26] Thomas, M.E., Neuberg, J., 2012. What makes a volcano tick - a first explanation of deep multiple seismic sources in ascending magma. Geology 40, 351–354.

[27] Wang, R., 1999. A simple orthonormalization method for stable and efficient computation of green's functions. Bulletin of the Seismological Society of America 89, 733–741.

[28] White, R.S., Drew, J., Martens, H.R., Key, J., Soosalu, H., Jakobsdóttir, S.S., 2011. Dynamics of dyke intrusion in the mid-crust of iceland. Earth and Planetary Science Letters 304, 300–312.

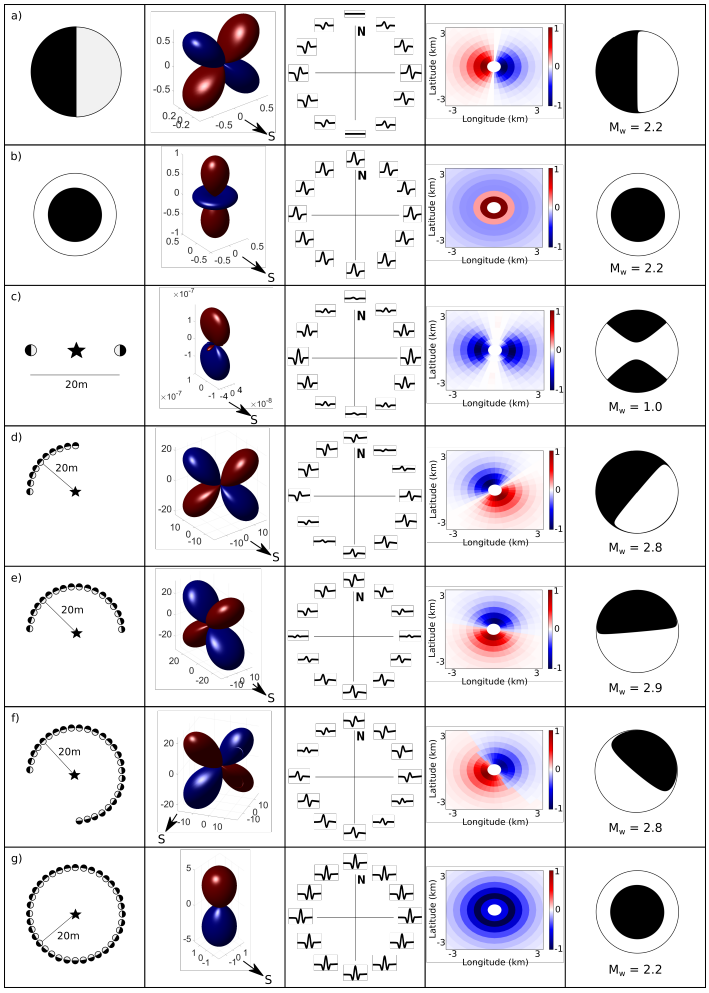

Figure 5: Summary of results obtained for forward and inverse modelling showing in columns: the rupture inspected, radiation pattern calculated, waveforms in all directions, polarisations at surface and moment tensor solution. a) DC point source; waveforms are represented by the derivative of the slip on the fault. The inversion retrieve accurately the MT solution, geometry and magnitude. b) CLVD point source; waveforms are represented by the derivative of the slip on the fault. The inversion retrieves accurately the MT solution, geometry and magnitude. c) Dyke source; waveforms are represented by the second derivative of the slip on the fault. Radiation patterns, which assume simultaneously arriving contributions, are not in accordance with polarisations at surface. The inversion process does not retrieve the correct moment tensor solution and the magnitude is underestimated. d-f) 1/4-, 1/2- and 3/4-ring ruptures show similar results than a DC with different azimuth (Fig. 7) The inversion process supports the similarities between these ruptures and DC solutions; however, the magnitudes are underestimated. g) full-ring source; waveforms are represented by the second derivative of the slip on the fault. Radiation patterns, as for the case of the dyke fault, are not in accordance with polarisations at surface. The inversion process does not retrieve the correct moment tensor solution and the magnitude is underestimated. The representation of the MT solution is misleading since the correct solution is an implosion (the representation only shows the deviatoric components). For interpretation of the colour scales in this figure, the reader is referred to the web version of this article.

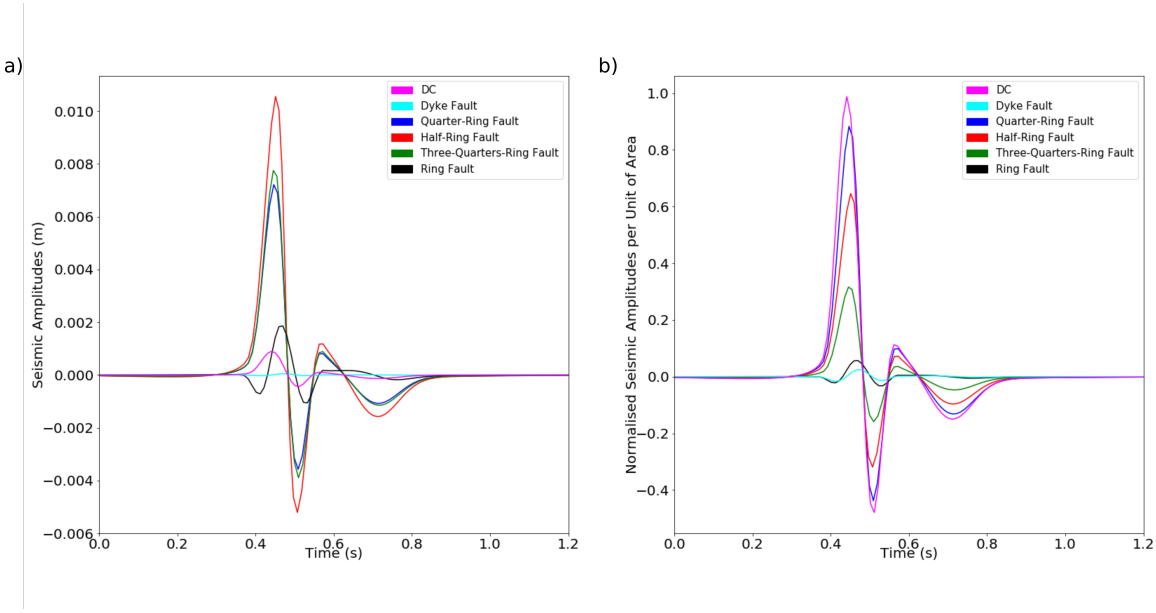

Figure 6: a) Raw amplitudes obtained from modelling. b) Normalised amplitudes by area of rupture, it can be understood as the radiation efficiency of each source geometry (For interpretation of the colour legends for each plot, the reader is referred to the web version of this article).

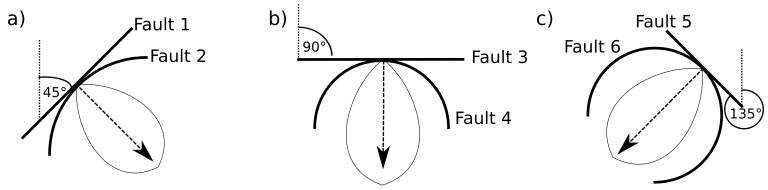

Figure 7: Six different faults with their direction of maximum amplitude. This direction is parallel to the symmetry axis of the curved faults and perpendicular to the planar faults. Left: Similarities between 1/4-ring rupture and 45° striking planar fault. Centre: Similarities between 1/2-ring rupture and 90° striking planar fault. Right: Similarities between 3/4-ring rupture and 135° striking planar fault.

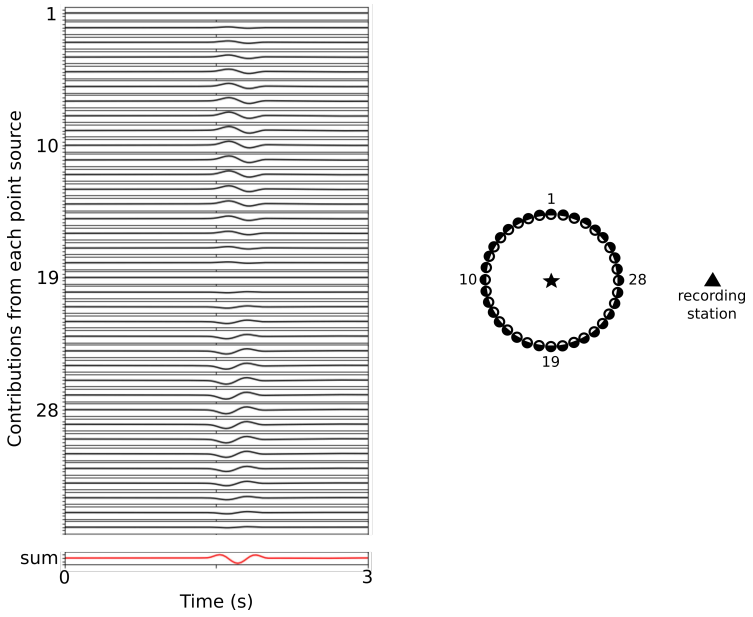

Figure 8: Contributions of single sources representing a full-ring rupture and the resulting waveform (red) at a recording station to the east. Note that single waveforms differ according to the radiation pattern. The resulting waveform (sum) exhibiting an apparent time derivative is due to slight differences in travel time between contributing sources. Sketch on the right not to scale.

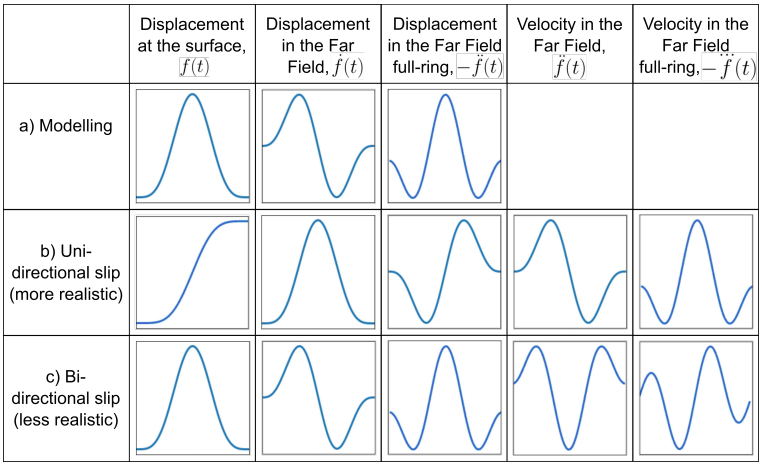

Figure 9: Waveforms expected for forward modelling, using a source described through a Moment Tensor for: a) Case modelled. b) Uni-directional slip, note that the velocity record in the far field for the full-ring rupture is similar to the displacement produced by a full-ring fault in our modelling. During volcanic unrest the magma follows an upward movement, so this is a more realistic case for LP trigger rupture. c) Bi-directional slip. This would represent magma moving upwards and downwards as part of the same rupture process, which during unrest is unlikely.

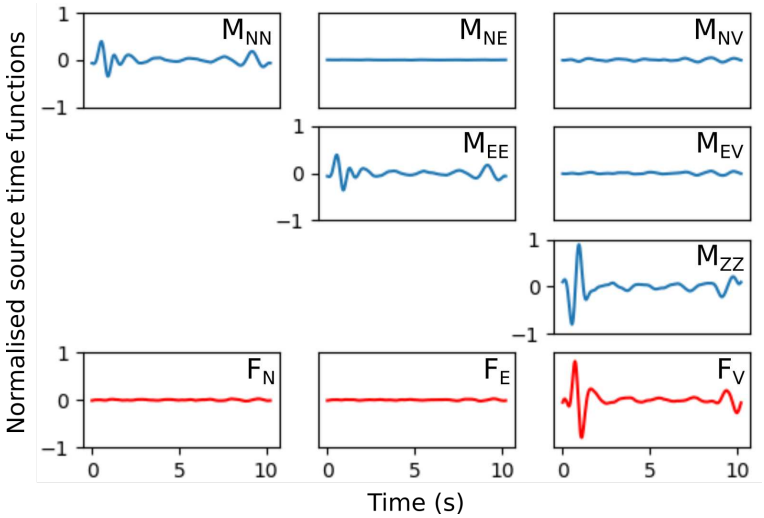

Figure 10: Source time functions for moment tensor components and single forces. The results show a vertical CLVD and a single force pointing downwards.